ORNL/TM-12011

ornl

OAK RIDGE NATIONAL LABORATORY

MARTIN MARIETTA

Phase Distribution Measurements in Narrow Rectangular Channels Using Image-Processing Techniques

C. L. Bentley
A. E. Ruggles

MANAGED BY
MARTIN MARIETTA ENERGY SYSTEMS, INC.
FOR THE UNITED STATES
DEPARTMENT OF ENERGY

ORNL/TM-12011

Engineering Technology Division

Phase Distribution Measurements in Narrow Rectangular Channels Using Image-Processing Techniques

C. L. Bentley
A. E. Ruggles

DATE PUBLISHED: JUNE 1992

Prepared for
Office of Energy Research
Basic Energy Sciences

Prepared by the
OAK RIDGE NATIONAL LABORATORY
Oak Ridge, Tennessee 37831-6285
managed by
MARTIN MARIETTA ENERGY SYSTEMS, INC.
for the
U.S. DEPARTMENT OF ENERGY
under Contract DE-AC05-84OR21400

CONTENTS

LIST OF FIGURES

LIST OF TABLES

NOMENCLATURE

C	coefficient
D	diameter
g	gravitational acceleration
h	distance between taps
j	superficial velocity
K_1	multiplier
l	liquid
R	radius
s	gap of channel
U	velocity
w	span of channel
α	air fraction
ρ	density
σ	surface tension
δ_f	liquid film thickness

Subscripts

g	gas
h	hydraulic
l	liquid
p	pressure
∞	infinite

PHASE DISTRIBUTION MEASUREMENTS IN NARROW RECTANGULAR CHANNELS USING IMAGE-PROCESSING TECHNIQUES

C. L. Bentley
A. E. Ruggles

ABSTRACT

Phase distribution of air–water flow in a narrow rectangular channel is examined using image-processing techniques. Ink is added to the water, and clear channel walls are used to allow high-speed, still photographs and video tape to be taken of the air–water flow field. Flow field images are digitized and stored in a Macintosh IIci computer using a frame grabber board. Local grey levels are related to liquid thickness in the flow channel using a calibration fixture. Image-processing shareware is used to calculate the spatially averaged liquid thickness from the image of the flow field. Time-averaged spatial liquid distributions are calculated using image calculation algorithms. The spatially averaged liquid distribution is calculated from the time-averaged spatial liquid distribution to formulate the combined temporally and spatially averaged liquid fraction values. The temporally and spatially averaged liquid fractions measured using this technique compare well to those predicted from pressure gradient measurements at zero superficial liquid velocity.

---

1. INTRODUCTION

Many fuel assemblies for high-flux research reactors are cooled by systems of parallel narrow rectangular channels. A schematic of the fuel assembly of one such reactor, the High Flux Isotope Reactor (HFIR) located at Oak Ridge National Laboratory, is shown in Fig. 1. A typical cooling channel for the fuel assembly has a span of 84 mm and a gap of 1.27 mm. The length of the cooling channel is 610 mm.

HFIR is cooled by single-phase forced convection under normal operating conditions. However, two-phase forced convection or two-phase mixed convection can occur in the fueled region as a result of some hypothetical accidents. Such flow conditions would occur only at decay power levels. The system pressure would be ~0.15 MPa in such circumstances.

Griffith (1964) examined adiabatic two-phase flows in several flow geometries, including rectangular channels, and developed a relationship between the gas and liquid superficial velocities and the channel average void fraction. Griffith observed that the channel span was the more important dimension in modeling two-phase slug flows in channels. Griffith's model has been used successfully to predict data taken in rectangular channels with various cross sections (Griffith 1964, Mishima et al. 1988, Sadatomi and Sato 1982, Jones and Zuber 1978, and Moujaes and Dougall 1985). His formulation was originally developed for the fully

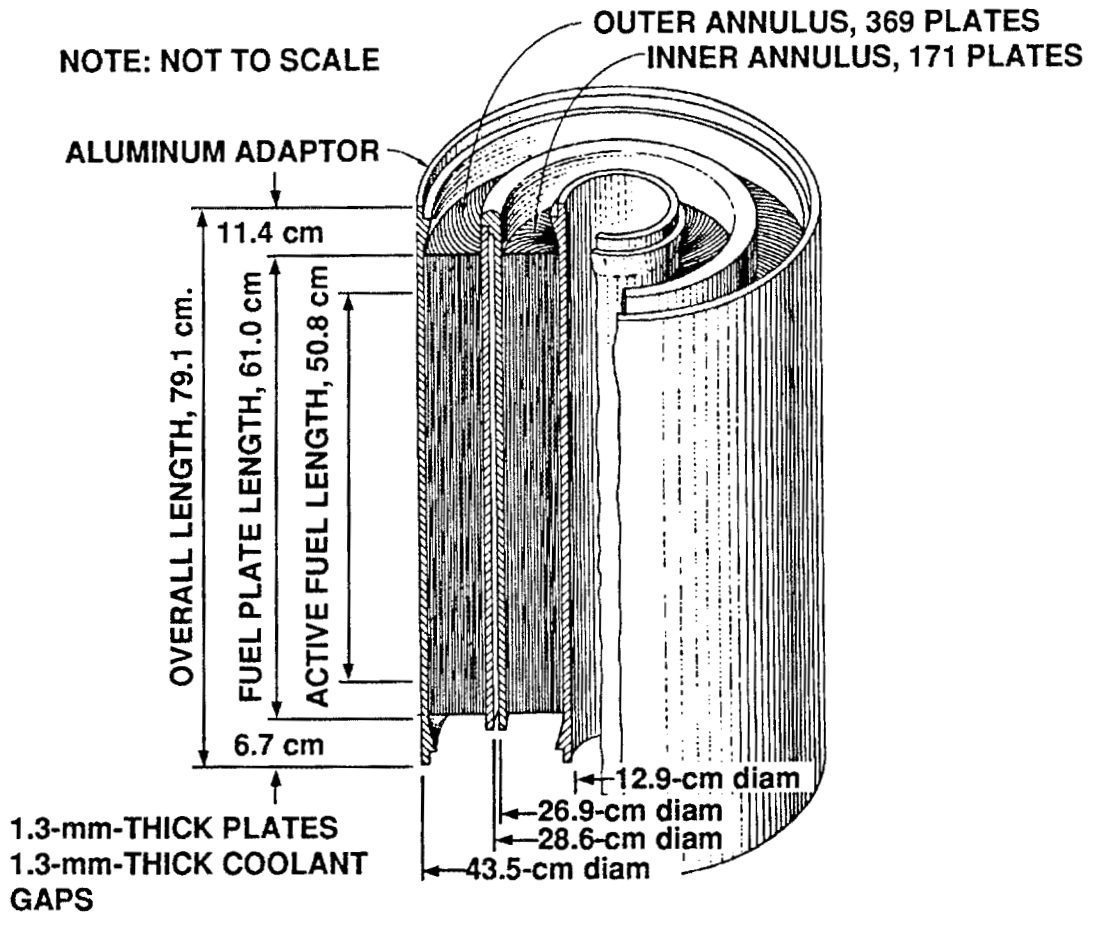

Fig. 1. High Flux Isotope Reactor fuel assembly.

developed slug flow regime. However, it has performed well for void fractions ranging up to 80%.

The HFIR fuel assembly cooling channels have a length-to-span ratio of 8. Thus, the two-phase flow conditions in the fuel assembly may not be well developed. The HFIR channel cross section has a span-to-gap ratio of 66. This is beyond the maximum span-to-gap ratio of 20.8 examined in previous work (Mishima et al. 1988). The unusual dimensions of the channel cross section and the developing nature of the flow challenged the applicability of the model proposed by Griffith (1964). This study was conducted to verify and/or develop models for use in the analysis of low-mass flux cocurrent two-phase upflow situations in the HFIR fuel assembly.

2. EXPERIMENTAL FACILITY

A single, unheated channel with a cross section of 127.0 by 1.76 mm was constructed from two sheets of Lexan separated by spacers, as shown in Fig. 2. Two steel bar assemblies supported the two Lexan sheets externally (Fig. 3). Each assembly was milled flat on the side

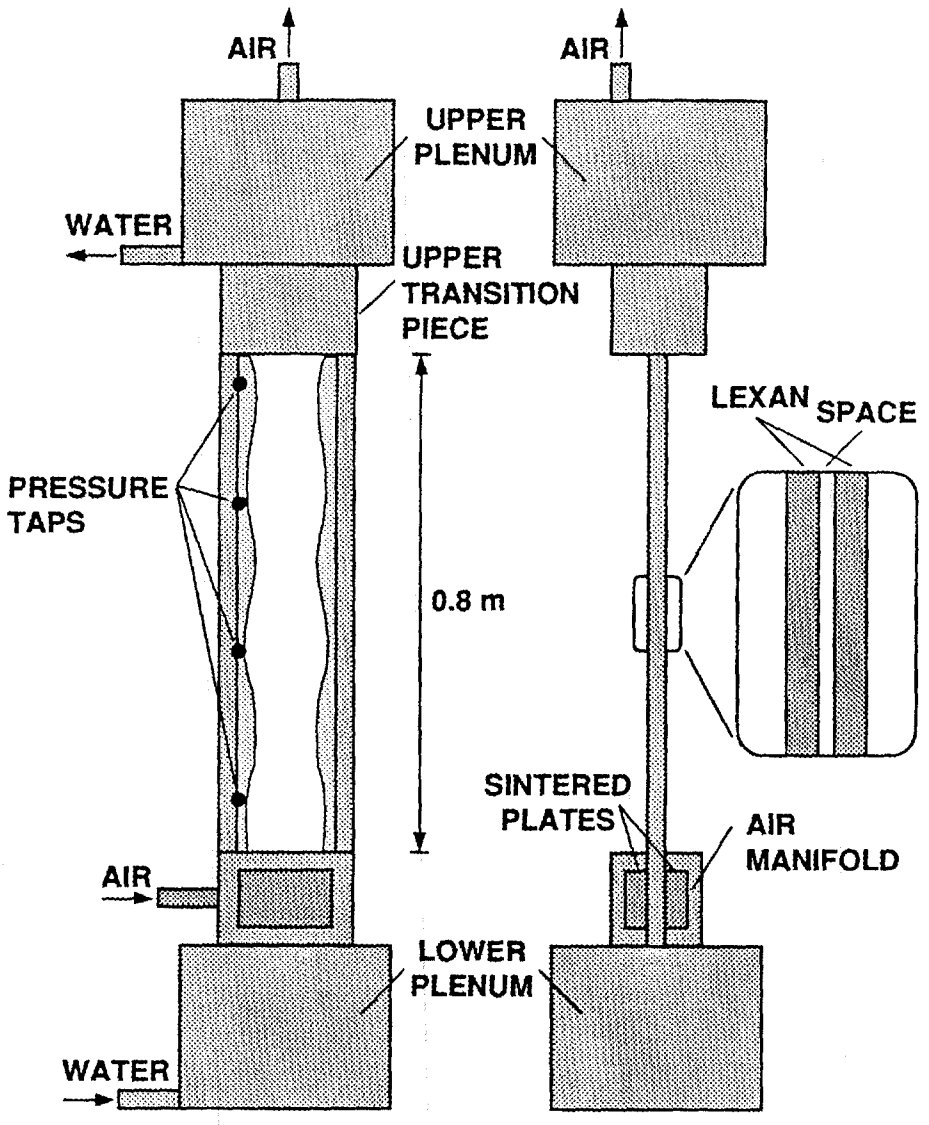

Fig. 2. Experimental test section.

contacting the Lexan and held in place by eight "C" clamps positioned four along each side of the channel. This ensured that the Lexan sheets remained flat and parallel. The average gap in the assembly was checked by draining segments of the channel into a buret and found to be 1.76 ± 0.03 mm. The channel width was 127.0 mm. The channel inlet and exit plenums were 203 mm in diameter and 250 mm tall. The channel inlet and exit connections to the plenums were sharp edged.

Four rotameters measured the volume flow of air to two porous sinter plates mounted in stainless manifolds at the bottom of the flow channel. The sinters, mounted flush to the inside surface of the channel wall, extended across the entire span of the channel. The total length of the flow channel was 1.35 m from the bottom of the porous sinter to the upper plenum. Flow visualization studies were possible along the channel from a height of 0.2 to 1.0 m. The top

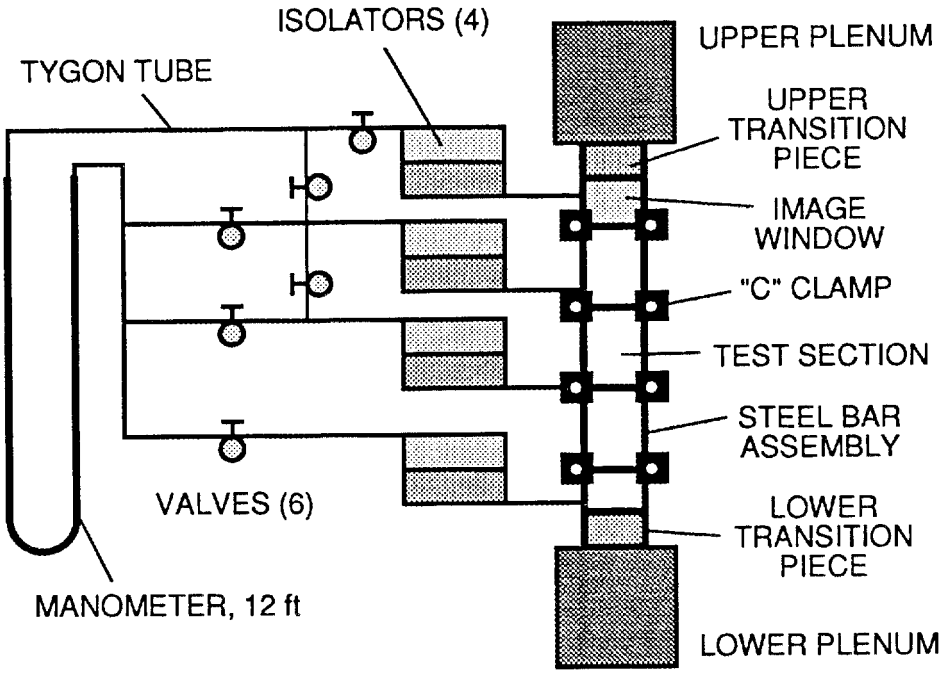

Fig. 3. Facility.

0.15 m had aluminum walls to aid in the construction of the junction with the upper plenum. A bank of four rotameters accomplished liquid-mass flux measurements. A high-head centrifugal pump circulated the liquid flow through the channel. The metering valves upstream of the rotameters provided most of the pressure drop in the system, ensuring a steady liquid-mass flux through the channel. All rotameters were calibrated, and reported air rotameter volume measurements were corrected for variations between the calibration pressure, operation pressure, and in-channel pressure. The metered air and water supplies were connected to the channel to study cocurrent upflow in these tests. The maximum uncertainty in the reported air volume flux was ±7%.

Local pressure gradients were measured using a single air–water manometer. This manometer could be connected to any pair of four pressure taps located along the channel. The air legs of the manometer were isolated from the flow in the channel by four reservoirs of large diameter (Fig. 3). The pressure taps were located at the edge of the channel span to prevent air from entering the manometer lines during operation. Care was taken to check the liquid portions of the manometer lines for air before taking pressure measurements. The pressure differences measured by the manometer were correct to within ±25 Pa.

The liquid used in these experiments is 1000 parts water to 2 parts ink by volume. The surface tension of the water and ink was measured consistent with ASTM 1590-60 as 66.4 dyn/cm. The hydraulic diameter of the test channel was scaled to match a HFIR cooling channel with steam–water flow at 0.15 MPa based on the Eötvös number,

$$E\ddot{o} = \frac{gD_H^2(\rho_l - \rho_g)}{\sigma} \quad . \tag{1}$$

3. MEASUREMENT TECHNIQUES

A Sony DXC-325 shuttered video camera was used to record the phase distribution images across the span of the channel. A uniform diffused light source was positioned behind the flow channel. Shutter speeds of either 1 or 2 ms were used. Figure 4 shows the arrangement of the video camera, channel, and light source.

The video images were transferred to a Macintosh IIci computer using a frame grabber card manufactured by Data Translation (Model Number DT2255). The images were analyzed using the Image 1.33q software available free through the National Institutes of Health (NIH) Research Services Branch.* Final spatial resolution of the digitized image of the flow field was 0.3 by 0.3 mm per pixel.

The relationship between grey level and liquid thickness was determined using a calibration section constructed from Lexan (Fig. 5). The calibrator was filled with liquid from

*The Image 1.33q software is available at the network address: FTP Sumex-Aim. Stanford. EDU. Anonymous users can access shareware under the password "Guest," using standard UNIX commands. The Image file is listed under the root directory application.

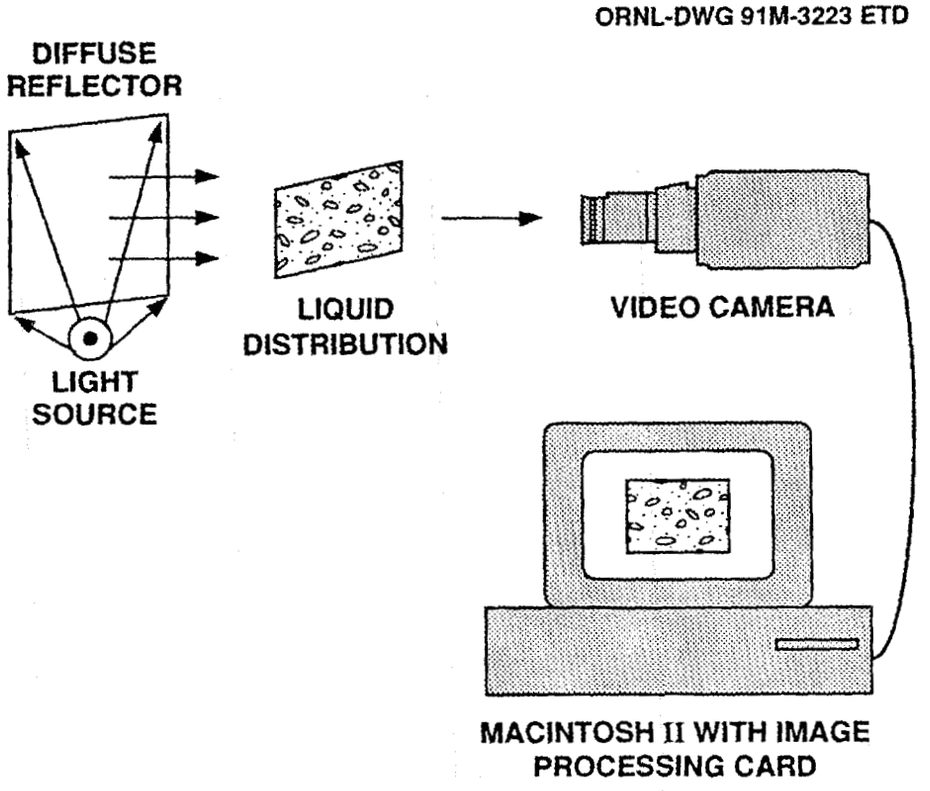

Fig. 4. Phase distribution image capture technique.

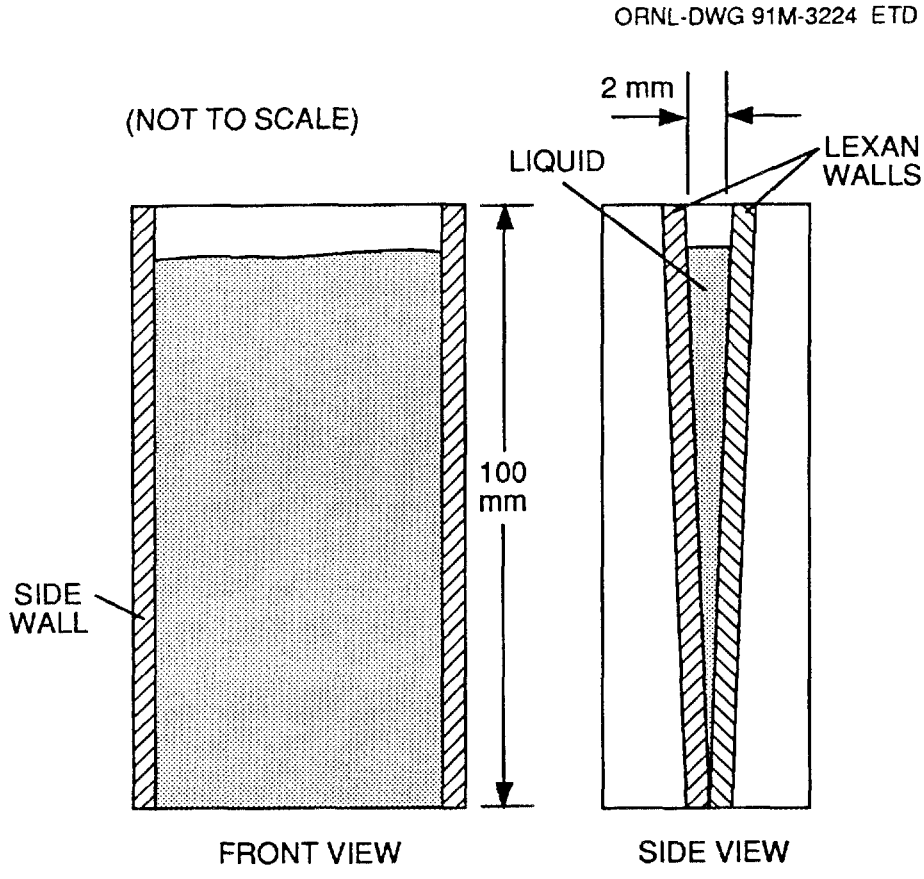

Fig. 5. Fixture used to relate liquid thickness to grey level.

the flow facility and recorded using the same technique used for the images of the channel. The digitized image of the calibration fixture was then used to relate grey levels to liquid thickness (Fig. 6). Note that the calibrator walls were inclined just 1.2° to one another, making the influence of refraction on the calibration results negligible. A linear relationship existed between the grey level and liquid thickness that persisted over a wide range of exposure conditions. The distribution of grey levels in the images of the flow field were converted to a distribution of liquid thicknesses using the image calibration feature in the Image 1.33q software. Images of the flow section with full liquid and full air were recorded with each photographic session to verify the spatial uniformity in lighting and to establish the full liquid and full air grey levels for the calibration of grey level to liquid thickness. The spatial variation in the measured liquid thickness due to spatial variations in the lighting never exceeded ±6% of the total channel gap. Note that the average grey level over the entire spatial field of the image was used for the calibration of liquid thickness to grey level. Therefore, the variation in the temporally and spatially averaged liquid fraction values will be less than the variation in the local spatial liquid thickness.

Five images taken at identical flow conditions were averaged to calculate time-averaged liquid fractions for each flow condition. All images reported here were taken at the top of the Lexan portion of the channel in the position shown in Fig. 3. The full width of the flow channel

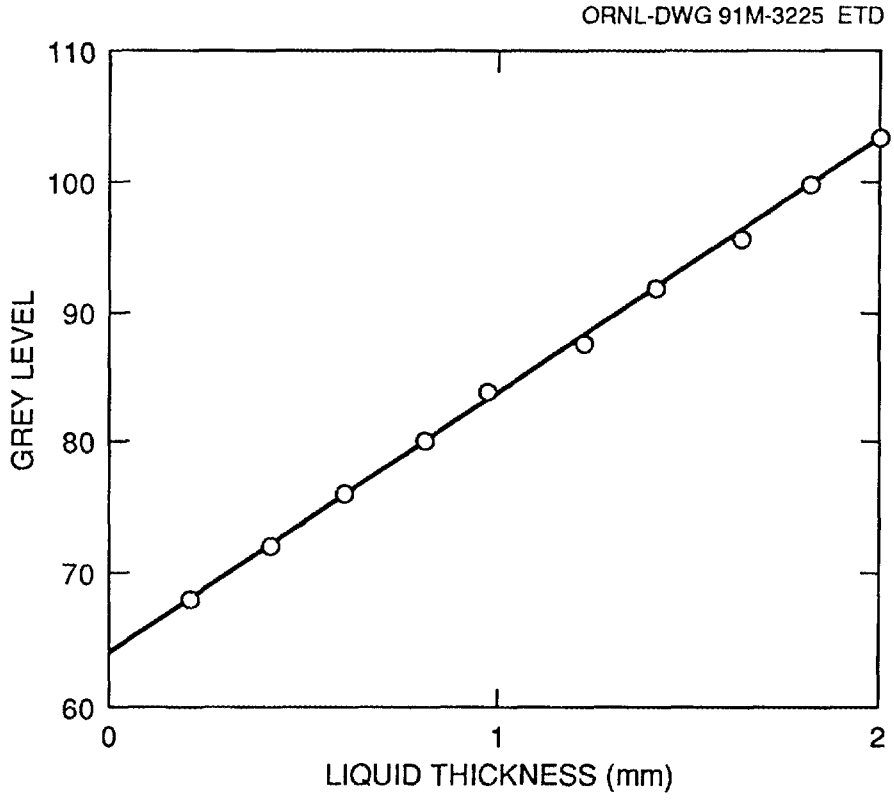

Fig. 6. Grey level vs liquid thickness.

was included in each image, and the image height included 100 mm of the channel height. Figure 7 depicts a typical image from each flow regime.

The channel average void fraction measured using the image-processing technique was compared against the void fraction calculated from the local pressure gradient. The local pressure gradient is related to the average void fraction by

$$\Delta p_{\text{channel}} = \left[(1-\alpha)\rho_l + \alpha\rho_g\right]gh \ . \tag{2}$$

This relationship holds when viscous wall drag is negligible; it is used here for data taken at zero liquid superficial velocity. Figure 8 compares the void fraction calculated using these two techniques.

The small spacing between the Lexan walls makes surface tension forces significant. Therefore, the liquid distribution across the gap of the channel tends to be either in the form of two very thin films resting on the channel wall or all liquid (Fig. 9). The thin, liquid film forms as a result of the pressure inside the disk being ~80 Pa greater than that in the liquid, where the pressure difference between the gas and liquid can be expressed approximately as a function of the surface tension and the minimum radius of curvature at the interface,

$$p_g - p_l = \sigma(1/R_{\text{min}}) \ . \tag{3}$$

ORNL PHOTO 12215-91

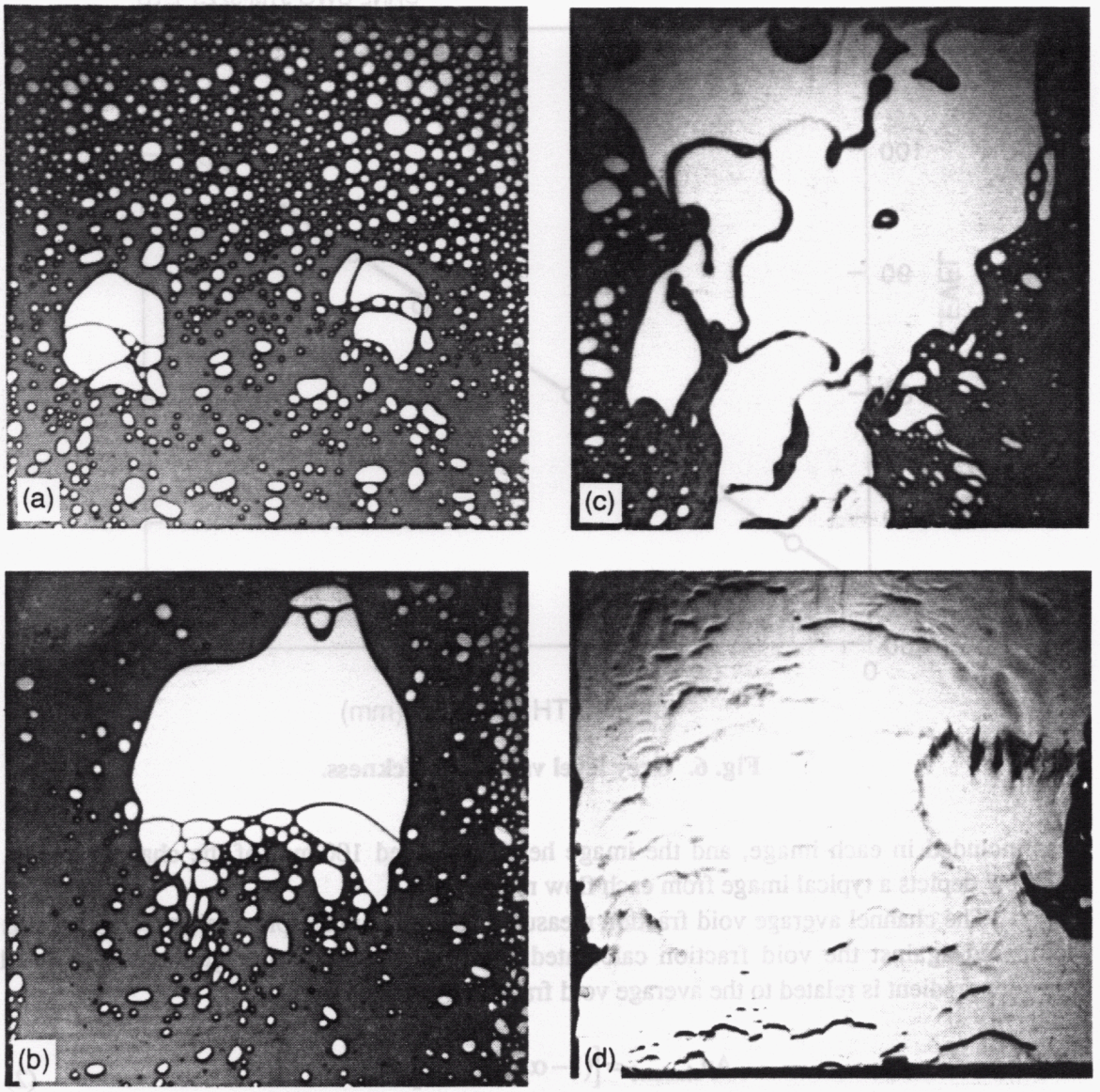

Fig. 7. Typical flow regime image of (a) disk flow, (b) slug flow, (c) churn flow, and (d) annular flow.

The minimum radius of curvature can be taken as half the spacing between the Lexan channel walls. Dark lines appear around disks as a result of the refraction of light at the liquid–air interfaces near the disk perimeter. Figure 10 shows the variation in the grey level across a section of a disk. Those grey levels exceeding the grey level corresponding to all liquid are due to refraction and reflection of light at the perimeter of the disk. Average void fraction values were calculated by setting the maximum allowable grey level at the value corresponding to when the channel is full of liquid. The void fraction values calculated in this manner did not vary significantly from those calculated without the correction when the disk diameters exceeded 10 mm on average. However, this phenomenon is responsible for the failure of the

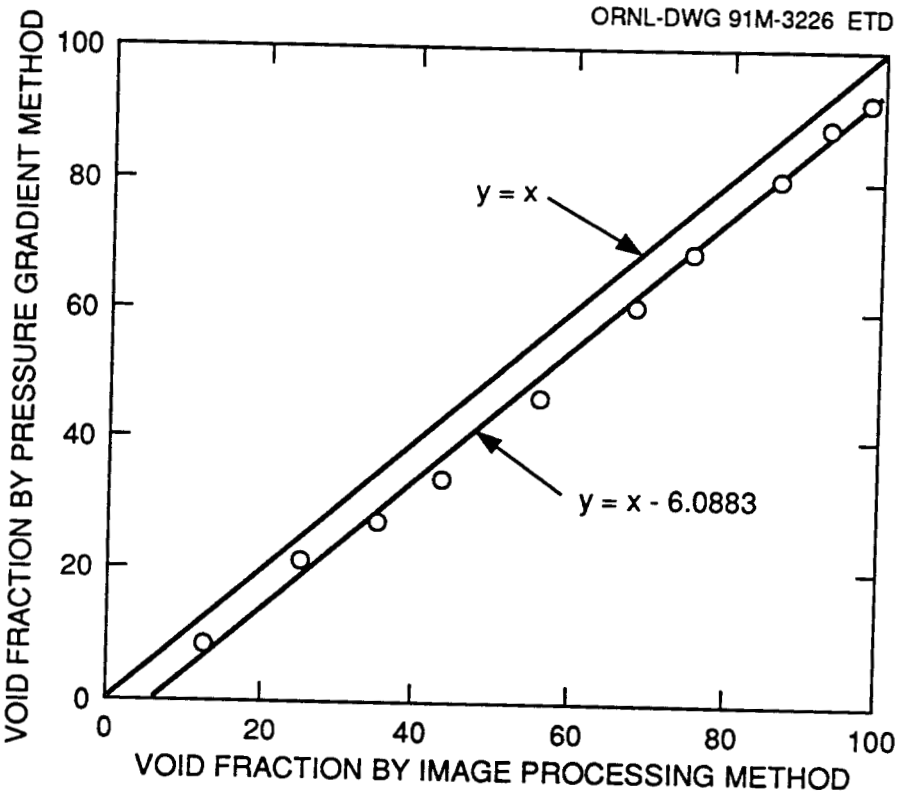

Fig. 8. Comparison of void fraction measurement performance.

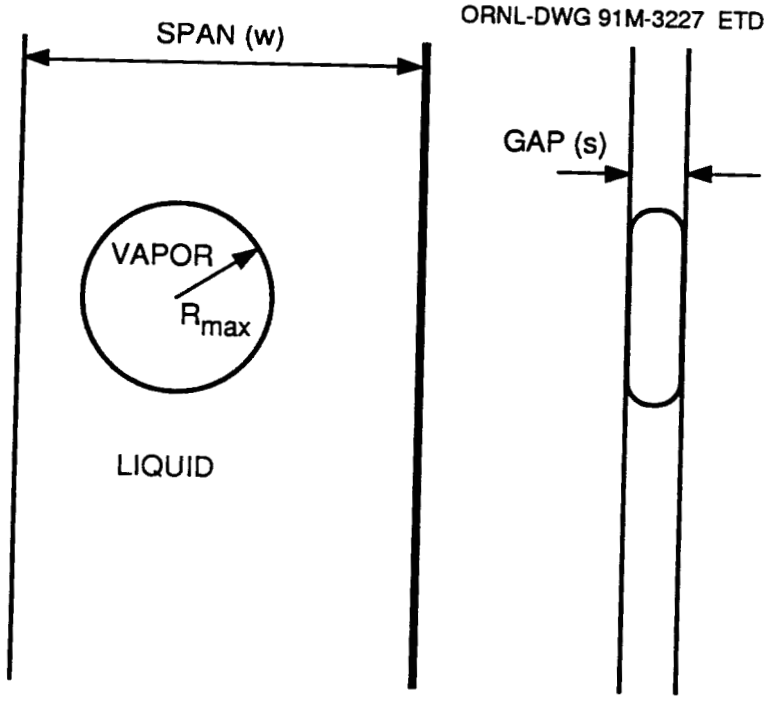

Fig. 9. Idealized disk flow regime model.

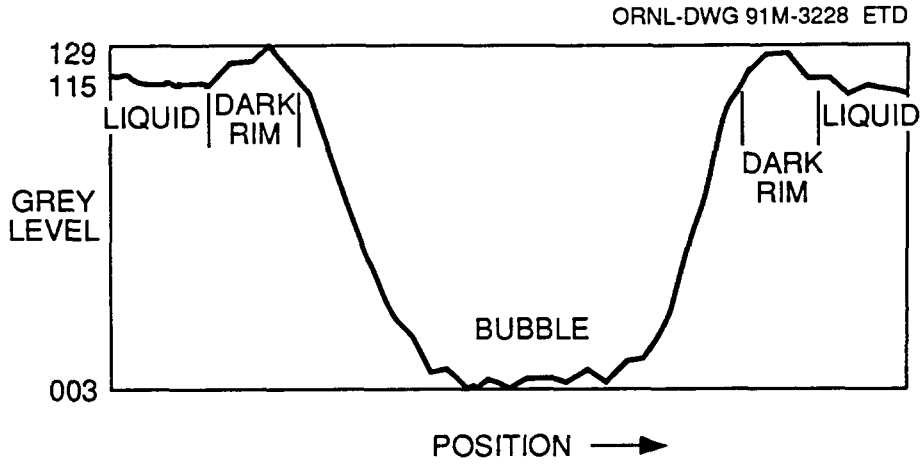

Fig. 10. Position vs grey level across a bubble with a dark rim.

present image-processing technique in predicting the channel-average void fraction in the bubbly flow regime. More complicated image-processing algorithms of the type employed by Hassan and Blanchat (1990) allow accurate calculation of the average void fraction in the bubbly flow regime.

4. MEASURED DRIFT FLUX PERFORMANCE

Figure 11 shows the calculated air velocity as a function of the total superficial velocity, where the air velocity is given as

$$u_g = \frac{j_g}{\alpha} \quad , \tag{4}$$

and the total superficial velocity is defined as

$$j = j_g + j_l \quad . \tag{5}$$

A general formulation of the drift flux model was developed by Wallis (1969) for slug flows in the form

$$U_g = C_1 j + C_2 U_\infty \quad , \tag{6}$$

where

$$U_\infty = K_1 \sqrt{gw\Delta\rho / \rho_l} \quad .$$

The coefficient C_1 is given in a table by Griffith (1964) as a function of the aspect ratio of the channel cross section. The coefficient C_1 is equal to 1.13 for the channel cross section tested here. The coefficient C_2 is usually taken as unity for fully developed slug flows when the liquid slugs are in the turbulent regime (i.e., $Re_j > 8000$). The velocity, U_∞, is defined as the rise velocity of a gas slug through a stagnant liquid column. Griffith gives the value for K_1 as a function of the aspect ratio of the channel cross section. The value for K_1 is 0.23 for channels

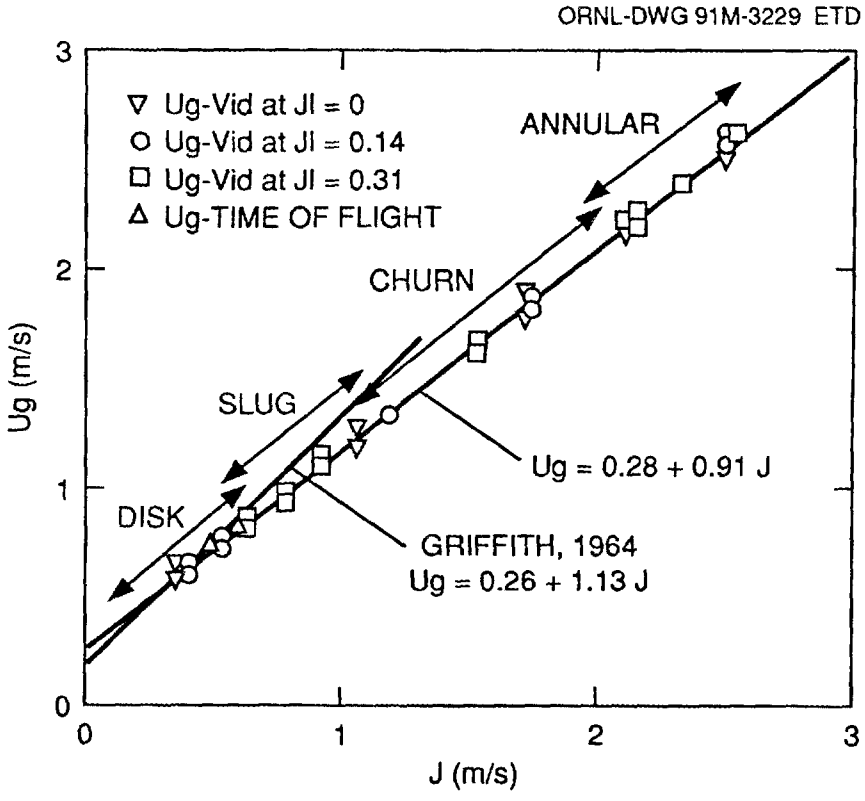

Fig. 11. Drift flux performance.

with very large ratios of span over gap, such as that tested here. Note that this limiting value for K_1 was taken from an analytical study of rising plane bubbles by Birkhoff and Carter (1957). Figure 11 plots the model from Griffith (1964) and predicts the data in the disk and slug regime reasonably well.

Several gas velocity measurements were made in the disk and slug regimes using time of flight measurement techniques. These measurements are also reported in Fig. 11 and are consistent with the gas velocities measured using the image-processing technique.

5. FLOW REGIMES

The flow regime transitions in Fig. 11 are for zero superficial liquid velocity. However, the position of the flow regime transitions did not change significantly for the range of superficial liquid velocities examined in these tests.

The flow regimes in narrow channels are somewhat different from those that occur in tubes and annuli. Conventional bubbly flow exists when the bubble diameters are less than the channel gap. However, bubbles with diameters approaching the channel gap dimension assume disk shapes as they become trapped between the channel walls (Fig. 9). The disks remain relatively round until their diameter approaches 20 mm. Larger disks with flat bottoms become apparent as the superficial gas velocity is increased.

The beginning of the disk-to-slug flow transition is chosen to correspond to when the large disks in the flow have widths greater than half the span of the channel, with the flow observations being made at the top of the channel. Smaller disks in the wake of larger disks rapidly catch and coalesce with the larger disks at the disk-to-slug flow transition. Therefore, the nature of the flow field varies considerably along the length of the Lexan channel. This behavior continues throughout the slug flow regime.

The slug-to-churn flow regime transition was chosen when the liquid slugs became much shorter than the gas slugs. The liquid slugs become very transient at this transition due to rapid coalescence of the gas slugs. Liquid bridges across the channel span are alternately formed and broken in the churn flow regime. The liquid bridges are connected and fed by two rapidly falling liquid streams at both sides of the channel span. While the slug flow regime showed significant variation along the height of the channel, the churn flow regime assumed a fully developed form within 200 mm of the beginning of the clear section of the channel.

The churn-to-annular flow transition on Fig. 11 denotes when liquid slugs no longer bridge the channel span as the superficial gas velocity is further increased. The liquid still tends to be either completely bridging the gap between the Lexan channel walls or residing in two thin (i.e., δ_f equal to 0.2 mm on average) smooth films, fully wetting the Lexan walls. Waves form on the liquid film, wetting the Lexan channel walls as the superficial gas velocity approaches 1.5 m/s. The liquid still falls in streams at both sides of the channel span. Occasionally a large wave will form in one of the falling streams. The liquid in the crest of the wave is entrained in the gas core and carried upward. A typical wave of this type is shown in Fig. 7. Further increase in the liquid superficial velocity results in channel dry-out under conditions of zero superficial liquid velocity.

Figure 12 depicts the distribution of liquid across the span for the annular flow image in Fig. 7. The liquid film thickness on the Lexan channel wall is minimum at the centerline of the channel span. Note that the majority of the liquid in the channel actually resides in the film on the Lexan walls.

6. FUTURE WORK

Further investigation is needed to understand why the image-processing technique consistently predicts slightly higher values of void fraction than the hydrostatic pressure technique from Eq. (2). A separate, independent technique for measuring liquid film thicknesses may be used for this task.

A study is planned of the velocity and temperature fields downstream of a partial inlet flow blockage of a HFIR fuel element cooling channel. The image capture hardware and image-processing software will be used in conjunction with thermochromic film to measure the spatial temperature variation of the heated wall downstream of a blockage.

7. CONCLUSIONS

The image-processing technique developed herein is useful for gathering information on the void fraction for adiabatic flows in narrow, rectangular channels. The technique is most easily employed for flow situations in which the surface tension controls the liquid distribution between the transparent walls of the channel.

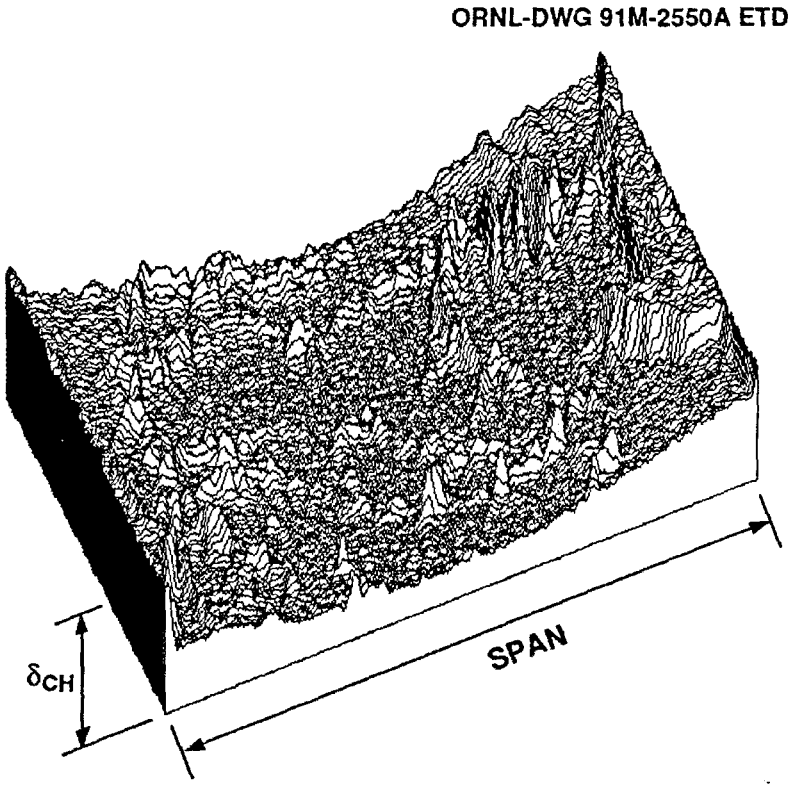

Fig. 12. Liquid distribution for annular flow.

Data on the liquid distribution across the channel span can also be obtained using this technique. Data on the distribution of the liquid for the annular flow regime could support modeling of interfacial drag terms during cocurrent and countercurrent annular flow. Current models assume all the liquid is in two films on either side of the channel span, due to Mishima and Nishihara (1984) and Cheng (1991). Ruggles (1990) proposed a model in which the annular countercurrent flow in the channel was modeled as two sets of planar films, with half of the liquid in the films across the channel gap and half in the films across the channel span. More realistic models are possible when information on the actual liquid distribution is available.

REFERENCES

Birkhoff, G., and Carter, D. 1957. "Rising Plane Bubbles," *J. Math. Mech.*, **6**(6), 776–779.

Cheng, L. Y. 1991. "Counter-Current Flow Limited CHF in Thin Rectangular Channels," *Proceedings 3rd ASME-JSME Thermal Engineering Joint Conference, Reno, Nevada, March 17–22.*

Griffith, P. 1964. "The Prediction of Low-Quality Boiling Voids," *J. Heat Transfer*, August, 327–333.

Hassan, Y. A., and Blanchat, T. 1990. "Two-Phase Bubbly Flow Velocity Measurements Using Pulsed Laser Velocimetry," ASME Winter Annual Meeting, Dallas, Texas, November 25–30, *Advances in Gas Liquid Flows*, Heat Transfer Division Vol. 155, FED Vol. 99.

Jones, O. C., and Zuber, N. 1978. "Slug Annular Transition with Particular Reference to Narrow Rectangular Ducts, Two-Phase Momentum, Heat and Mass Transfer," pp. 345–355 in *Chemical, Process, and Energy Engineering Systems, Vol. 1*, eds. F. Durst, G. V. Tsiklauri, and N. H. Afgan, Hemisphere Publishing Co., Washington, D.C.

Mishima, K., and Nishihara, H. 1984. "Flooding Velocities for Countercurrent Air–Water Flow in Thin Rectangular Channels," pp. 1–14 in *Annual Report of the Reactor Institute of Kyoto University, Kyoto, Japan, Vol. 17.*

Mishima, K., et al. 1988. "A Study of Air–Water Flow in a Narrow Rectangular Duct Using Image Processing Technique," Japan–U. S. Seminar on Two-Phase Flow Dynamics, Biwako Hotel, Ohtsu, Japan, July.

Moujaes, S., and Dougall, R. S. 1985. "Two-Phase Upflow in Rectangular Channels," *Int. J. Multiphase Flow*, **11**(4), pp. 503–513.

Ruggles, A. E. 1990. *Countercurrent Flow Limited (CCFL) Heat Flux in the High Flux Isotope Reactor*, ORNL/TM-11638, Martin Marietta Energy Systems, Inc., Oak Ridge Natl. Lab.

Sadatomi, M., and Sato, Y. 1982. "Two-Phase Flow in Vertical Noncircular Channels," *Int. J. Multiphase Flow*, **8** (6), pp. 641–655.

Wallis, G. B. 1969. *One-Dimensional Two-Phase Flow*, McGraw-Hill Book Company, New York.

Appendix A

MEASUREMENT UNCERTAINTY

A.1 VOID FRACTION FROM PRESSURE GRADIENT METHOD

The equation for the pressure gradient is given as a function of void fraction such that

$$\Delta P = \left[(1-\alpha)\rho_l + \alpha\rho_g \right] gh \quad . \tag{A.1}$$

Solving for the void fraction for situations in which the density of the vapor is much less than the density of the liquid, we see that

$$\alpha = 1 - \frac{\Delta P}{\rho_l g h} \quad . \tag{A.2}$$

For small, finite quantities we can write

$$\partial\alpha \cong \Delta\alpha \quad . \tag{A.3}$$

Now, using the chain rule for partial differential equations, we can write that

$$\Delta\alpha = \frac{\partial\alpha}{\partial\Delta P}\,\Delta(\Delta P) + \frac{\partial\alpha}{\partial h}\,\Delta h_t \quad . \tag{A.4}$$

From Eq. (A.3) we see that

$$\frac{\partial\alpha}{\partial\Delta P} = -\frac{1}{\rho_l g h_t} \tag{A.5}$$

and

$$\frac{\partial\alpha}{\partial h_t} = \frac{\Delta P}{\rho_l g h_T^2} \quad . \tag{A.6}$$

Substituting Eqs. (A.5) and (A.6) into Eq. (A.4), we obtain the following equation:

$$\Delta\alpha = -\frac{\Delta(\Delta P)}{\rho_l g h_T} + \frac{\Delta P \Delta h_T}{\rho_l g h_T^2} \quad . \tag{A.7}$$

Now, expanding the pressure uncertainty in Eq. (A.7) we see that

$$\Delta P = \rho_l g h_M \quad . \tag{A.8}$$

Using the chain rule for partial differentials, we obtain the following:

$$\Delta(\Delta P) = \frac{\partial \Delta P}{\partial h_M} \Delta h_M \quad . \tag{A.9}$$

From Eq. (A.8) we obtain

$$\frac{\partial \Delta P}{\partial h_M} = \rho_l g \quad . \tag{A.10}$$

Substituting Eq. (A.10) into Eq. (A.9), we obtain

$$\Delta(\Delta P) = \rho_l g \, \Delta h_M \quad . \tag{A.11}$$

Now, substituting Eq. (A.11) into Eq. (A.7), we see that

$$\Delta\alpha = - \frac{\Delta h_M}{h_T} + \frac{\Delta P \Delta h_T}{\rho_l g h_T^2} \quad . \tag{A.12}$$

So, from Eq. (A.12), Table A.1, and physical constants, we obtain the following value for the uncertainty of the void fraction from the pressure gradient method:

$$\Delta\alpha = 0.0157 \quad . \tag{A.13}$$

Table A.1. Quantitative data for uncertainty measurement

Quantity	Measurement	Uncertainty
V	27.45 cm^3	0.25 cm^3
h_M	45.72 cm	0.50 cm
h_T	25.41 cm	0.50 cm
S	12.70 cm	0.10 cm
A	2.16 cm^2	0.0027 cm^2

A.2 CROSS-SECTIONAL AREA

The cross-sectional area is given as a function of volume and channel span such that

$$A = \frac{V}{S} \quad . \tag{A.14}$$

Using the chain rule for partial differentials, we obtain the following equation:

$$\Delta A = \frac{\partial A}{\partial V} \Delta V + \frac{\partial A}{\partial S} \Delta S \quad . \tag{A.15}$$

From Eq. (A.14) we see that

$$\frac{\partial A}{\partial V} = \frac{1}{S} \tag{A.16}$$

and

$$\frac{\partial A}{\partial S} = -\frac{V}{S^2} \ . \tag{A.17}$$

Substituting Eqs. (A.16) and (A.17) into Eq. (A.15), we obtain the following equation:

$$\Delta A = \frac{\Delta V}{S} - \frac{V}{S^2} \Delta S \ . \tag{A.18}$$

Using Table A.1, we obtain the following value for the uncertainty of the cross-sectional area:

$$\Delta A = 0.00267 \ \text{cm}^2 \ . \tag{A.19}$$

Appendix B

REFRACTION OF LIGHT AROUND THE DISK EDGE

A problem was detected during the transformation from the Nikon 35-mm still shots to the computer files stored from the image-processing equipment. The disks appeared to have a dark rim or ring around their edges. These dark rings are displayed in the form of a column-averaged grey level plot taken across a disk with a dark ring (see Fig. 10). Note that the grey level of the dark rim is ~15 units higher than the liquid grey level; thus, the average grey level of the image is increased. Further, this increase in the average grey level of the image will decrease the channel-averaged void fraction of the image.

This dilemma was ultimately resolved as a light refraction problem upon a thorough study of the light transmission angle as a function of the interface angle of liquid to air. Refer to Fig. B.1 for the graphical representation of this work. Note that the light was completely refracted (i.e., no transmission) at an angle of 40° between the air and liquid interface relative to the channel wall. Further, the magnitude of this light refraction problem was found by plotting the volume fraction of the bubble with and without the black rim as a function of the disk radius. Given as Fig. B.2, the graph shows that as the disk radius increases, the volume fraction approaches 1; thus, the effects of the light refraction are diminished as the disk radius increases.

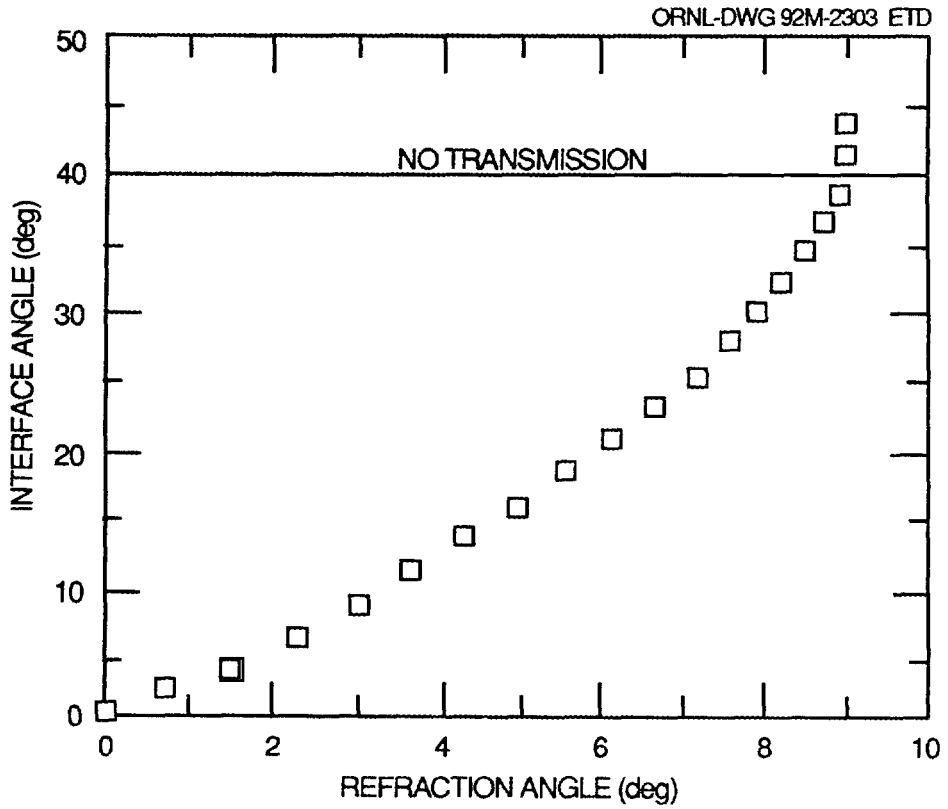

Fig. B.1. Refraction transmission angle.

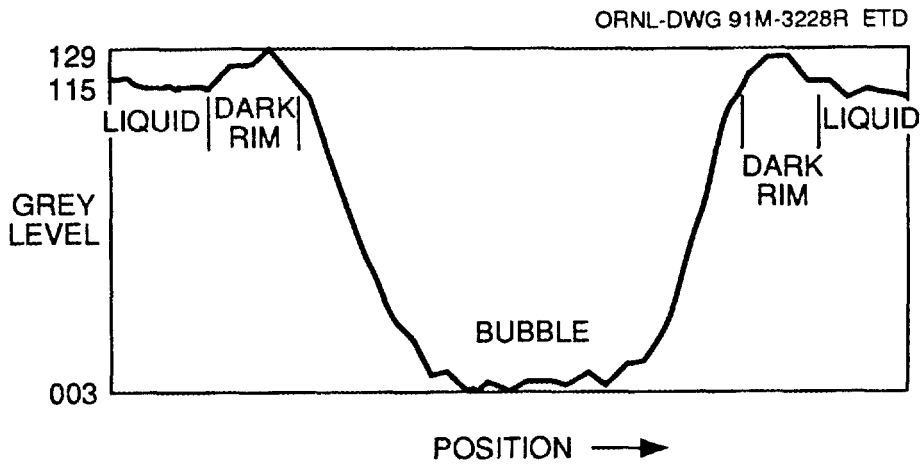

Fig. B.2. Effects of dark rim on volume fraction of bubble.

Finally, to eliminate the problem with the dark rings around the disks, two separate methods are being tested. First, the image-processing software allows the user to threshold the upper limit of the grey level; therefore, the software truncates any grey level that exceeds it to the threshold or a specified value. Unfortunately, the thresholding method is quite sensitive because the thresholding could at times truncate the grey levels of the liquid instead of the dark rings. Second, the image-processing software contains particle analysis capabilities. This allows the disk to be selected and uniformly given a desired grey level. This method is quite useful for the relatively larger disks but does not detect the disks when the radius is only slightly larger than the channel separation. Note that the particle analysis method is still being tested.

Internal Distribution

1–6. C. L. Bentley
7. D. H. Cook
8. W. G. Craddick
9. G. F. Flanagan
10. J. E. Jones Jr.
11. R. M. Harrington
12. D. G. Morris
13. F. R. Mynatt
14–19. A. E. Ruggles
20. E. W. Whitfield
21. G. L. Yoder
22. ORNL Patent Section
23. Central Research Library
24. Document Reference Section
25–26. Laboratory Records Department
27. Laboratory Records (RC)

External Distribution

28. C. Allison, EG&G Idaho, Idaho National Engineering Laboratory, P.O. Box 1625, Idaho Falls, Idaho 83415
29. S. Atkinson, EG&G Idaho, Idaho National Engineering Laboratory, P.O. Box 1625, Idaho Falls, Idaho 83415-7121
30. S. George Bankoff, Northwestern University, Chemical Engineering Department, Evanston, Illinois 60201
31. J. Block, Creare Incorporated, Etna Road, P.O. Box 71, Hanover, New Hampshire 03755
32. M. Buckner, Savannah River Laboratory, Aiken, South Carolina 29808
33. L. Y. Cheng, Brookhaven National Laboratory, Reactor Division, Building 703, Upton, New York 11973
34. Wallace Gambill, Route 5, Box 220, Clinton, Tennessee 37716
35. Y. Komori, Project Engineering Division, Japan Materials Testing Reactor Department, Oarai Research Establishment, Japan Atomic Energy Research Institute, Oarai-Machi, Higashi-Ibartaki-Gun, Ibaraki, 311-13, Japan
36. R. T. Lahey, Jr., 5048 JEC, Rensselaer Polytechnic Institute, Troy, New York 12180-3590
37. O. Manley, Department of Energy, Washington, DC 20555
38. K. Mishima, Research Reactor Institute, Kyoto University, Kumatori-Cho, Sennan-Gun, Osaka 590-04, Japan
39. J. P. Morin, Savannah River Laboratory, Aiken, South Carolina 29808
40. D. Ogden, Westinghouse Hanford Company, P.O. Box 1970, Richland, Washington 99352
41. B. Steinke, Los Alamos National Laboratory, P.O. Box 1663, Los Alamos, New Mexico 87545-551
42. R. P. Wadkins, EG&G Idaho, Idaho National Engineering Laboratory, P.O. Box 1625, Idaho Falls, Idaho 83415
43. G. Wallis, Thayer School of Engineering, Dartmouth College, Hanover, New Hampshire 03755
44. Office of Assistant Manager for Energy Research and Development, DOE, OR, P.O. Box 2008, Oak Ridge, Tennessee 37831-6269
45–54. Office of Scientific and Technical Information, P. O. Box 62, Oak Ridge, Tennessee 37831